ORIGINAL ARTICLE

Finite element investigation of IGSCC-prone zone in AISI 304L multipass groove welds

P. K. Taraphdar[1] · C. Pandey[2] · M. M. Mahapatra[1]

Abstract

AISI 304L stainless steel is most commonly used for spent nuclear fuel management; however, the welded joints of this steel are susceptible to intergranular stress corrosion cracking (IGSCC) under the influence of low-temperature sensitization. In the present research, the temperature history of two different groove designs (conventional and narrow groove) has been analyzed to ascertain the propensity of the weld zone to intergranular corrosion (IGC). 3D finite element models (FEMs) have been developed to retrieve the nodal thermal history and predict the region susceptible to IGSCC. The FEM results predicted a lower duration of exposure to the IGC temperature range for narrow groove design as compared to conventional design. The lower duration of exposure exhibits a lower propensity to chromium carbide precipitation and the tendency to IGSCC. The FEM analysis also has been used to observe the difference in the size of the region susceptible to IGSCC in the heat-affected zone of the respective weld designs. The predicted results obtained from the numerical analysis were validated by comparing the chromium carbide precipitation for both the groove designs.

1 Introduction

Austenitic stainless steels are used in petrochemical units and nuclear power plants where the material is susceptible to corrosion in working environments [1]. These steels have an excellent combination of properties like corrosion resistance, good weldability, strength, and ductility. Despite having significant advantages in physical properties and corrosion resistance, stress corrosion cracking (SCC) remains a drawback in welded joints of austenitic stainless steel. To avoid the sudden failure of stainless steel components, the cause of SCC has been studied by many of the researchers. Xin et al. studied the effect of post-weld heat treatment (PWHT) on the IGC resistance of SS316LN welded joints and observed that the IGC resistance decreased due to PWHT [2]. Kessal et al. investigated the effect of welding process parameters on the corrosion resistance of SS304L

welded joints. It was observed that the total number of weld passes and welding current significantly affects the corrosion resistance properties of the weldment [3]. Stress corrosion cracking is understood to be caused by the weld decay at the heat-affected zone (HAZ), commonly referred to as sensitization. Sensitization occurs due to the presence of a higher carbon percentage in the base material. The carbon atoms combine with chromium atoms at a temperature ranging from 550–800 °C and precipitate at the grain boundaries leaving Cr depleted zones [4]. These zones, later on, get affected by the corrosive agents and results in intergranular corrosion (IGC). Stress corrosion cracking (SCC) does not occur very close to the fusion boundary; instead, it occurs at the HAZ, which is adjacent to the partially melted zone (PMZ). The PMZ experiences a steep temperature gradient, which is not slow enough to nucleate chromium carbides. However, the HAZ away from the PMZ experiences a slow cooling rate to promote the formation of chromium carbides ($Cr_{23}C_6$), leading to intergranular stress corrosion cracking (IGSCC) [5]. Lee et al. encountered IGC in a multipass AISI 304 welded joint corresponding to a temperature range of 750 –960 °C, which is higher than the reported maximum temperature range for sensitization [5].

✉ C. Pandey
  jscapndey@iitj.ac.in; chandanpy.1989@gmail.com

1 School of Mechanical Sciences, Indian Institute of Technology, Bhubaneswar, Odisha 752050, India

2 Mechanical Department, IIT Jodhpur, Karwar, Rajasthan 342037, India

The precipitation of $Cr_{23}C_6$ strongly depends on the weight percentage of carbon and chromium present in the alloy. Austenitic stainless steels with carbon content higher than .05% are more susceptible to SCC when exposed to the range of sensitization temperature during service [6]. However, austenitic stainless steel with carbon content more than .04% failed in-service conditions in water reactor plants [8]. From past investigations, it has been observed that HAZ of pipe girth welds of boiling water reactor made of AISI 304 and 316 austenitic stainless steels is susceptible to IGSCC [7]. For better weldability, the 'L' grade of AISI 304 was introduced with less carbon wt% to avoid welding defects like weld decay. Reduction in carbon content in the material ensures fewer chances of sensitization. Among the AISI type 300 series, 304L stainless steel stands out to be one of the most commonly used materials as compared to other austenitic stainless steels due to its lower affinity to sensitization.

Kekkonen et al. have found that stainless steel welds are susceptible to IGC at the HAZ because of long time exposure at a temperature < 500 °C, the size of the carbides increases over time, whereas the total amount of carbides remained the same [9]. This phenomenon is known as low-temperature sensitization (LTS). AISI 304L austenitic stainless steel is frequently used in nuclear fuel storage canisters as an intervening loading unit for spent fuel management [10, 11]. The residual dissipating heat through convection regulates the LTS and SCC of the canister in a chloride-contaminated environment near the coastlines [11, 12]. The failure of nuclear waste carrying canister made of SS304/SS304L from the HAZ due to LTS-assisted IGSCC was reported [11]. The canister experienced a temperature range of 100–300 °C from the decaying radionuclides, which stimulated the growth of carbide nuclei. The application of welding promotes the nucleation of carbides, and the carbide nuclei strongly influence LTS.

Several studies have been conducted to develop a critical cooling rate (CCR) and time–temperature sensitization graphical plots to predict the sensitization possibilities during continuous cooling and heating. However, these plots are not appropriate where repeated heating and cooling are seen within the IGC temperature range in multipass welded joints. Suitable welding process and parameters with decent groove geometry of the welded joint should be adopted, which ensures reduced heat input and residual stress; so that the occurrence of IGSCC in SS304L welded components can be avoided. In this regard, the effect of weld groove geometries on the propensity of IGC was investigated using finite element modeling and experiments. In order to predict the IGC region in multipass welded joints, the transient temperature distribution along the HAZ was studied within a range of 750–960 °C for both the conventional and narrow groove welds.

2 Experimental procedure and material properties

Commercial purity grade AISI 304L austenitic stainless steel was chosen as base material for the present investigation. 300-mm-long and 110-mm-wide plates of 25 mm thickness were machined to make grooves on the edges. ER309L was used as the filler material because of its low carbon content, which can reduce the tendency of IGC. Chemical compositions of the base and filler material are given in Table 1 [13, 14]. Two sets of weld samples were prepared with conventional and narrow groove geometry. 1.5-mm root opening was kept during welding. The dimensions of the plates and groove geometries are given in Fig. 1a, b. The gas metal arc welding process (GMAW) was employed with DCEP polarity. Table 2 shows the parameters used in welding. The welding parameters were adjusted following the previous literature [13]. K-type thermocouple was placed at a distance of 10 mm away from the fusion boundary to validate the predicted temperature profile. ASTM A262 practice A was performed to examine chromium carbide precipitation. The electrolytic etching was done immersing the specimen in a 10% oxalic acid solution for 1.5 min with a current density of 1 A/cm^2.

3 Numerical modeling

Transient heat transfer analysis was done using the ABAQUS CAE software interface. The moving heat source of welding torch was defined using the USER SUBROUTINE FORTRAN program linked with the CAE interface. Two 3D finite element models were prepared for conventional and narrow groove geometry of AISI type 304L to predict the temperature distribution across the weldments. Figure 2a, b shows the cross-sectional view of the FE models along with their pass sequence. The steps carried out during the computational modeling of the

Table 1 Chemical composition of SS304L and ER309L

Materials	Chemical composition (wt%)							
	C	Mn	Si	Cr	Ni	P	S	Fe
SS304L	0.035	2.0	0.75	18.0–20.0	8.0–10.5	0.04	0.03	Balance
ER309L	0.011	1.6	0.36	23.77	13.19	0.013	0.001	Balance

Fig. 1 **a** Conventional groove, **b** narrow groove (measurements are in mm)
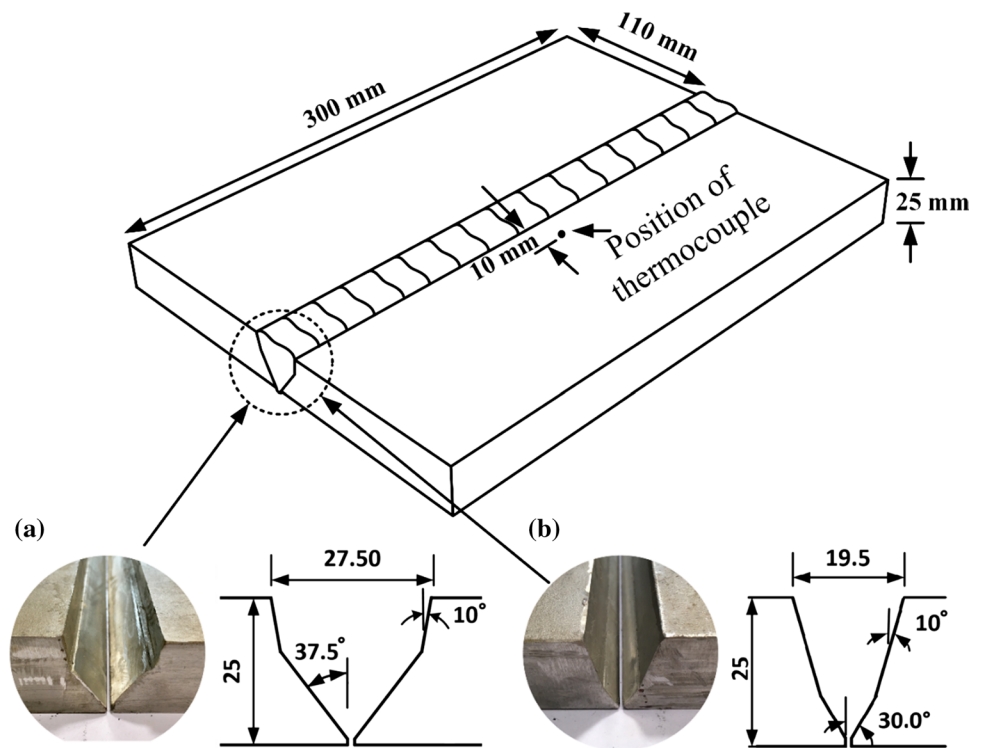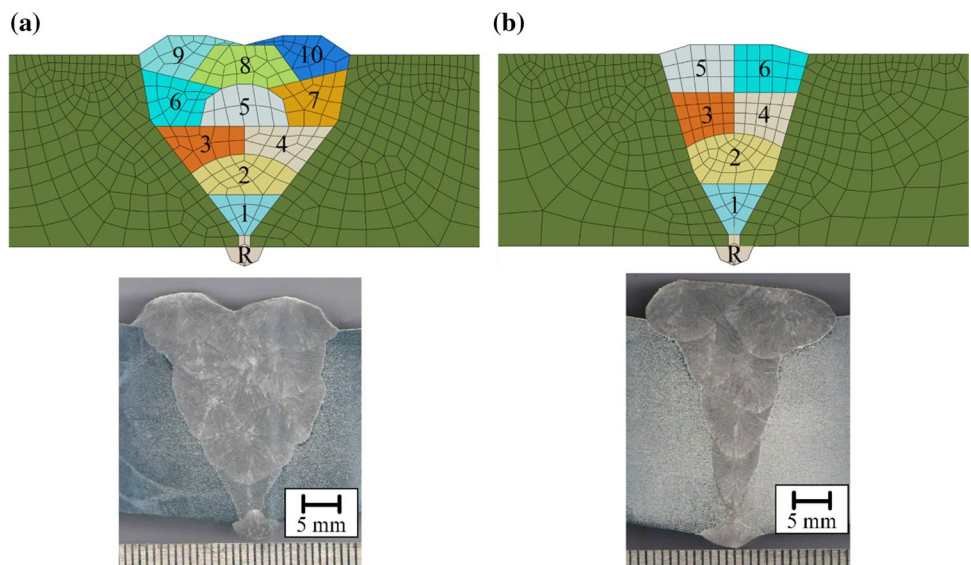

Table 2 Welding parameters

Specimen no.	Groove geometry	No. of passes	Passes	Current (A)	Voltage (V)	Travel speed (cm/min)	Argon gas flow (l/min)
1	Conventional	10	Root	180	24	78	10
			Weld	196–240	26–27	17	14
3	Narrow	6	Root	180	24	78	10
			Weld	196–248	26–27	20	14

Fig. 2 The sequence of weld passes and macrograph **a** conventional groove weld **b** narrow groove weld

weldments are shown in Fig. 3. Temperature-dependent material properties were selected to perform the simulation. Two separate material sections were created in the properties module to distinguish the weld filler material from the base material. The temperature-dependent thermal properties for both weld and filler material are given in Fig. 4 [15]. A biased meshing order was selected where the number of nodes of mesh gradually decreases from the axis of weld to the direction normal to the weld axis. Hexahedral mesh type and 8-node linear heat transfer brick (DC3D8) elements were employed for this thermal analysis. The smallest element size was taken as 1, and the total number of elements was 36112 and 31770 for conventional

and narrow groove joints, respectively. Mesh sensitivity analysis was done before the final analysis to substantiate the accuracy of the prediction model with a lower computational time. Convection and radiation were assumed for heat loss. The inter-pass temperature was maintained within 100–180 °C, as suggested [16]. The cooling time after root pass was employed as 100 s, and it was set as around 2600 s for the subsequent passes for both the welds to maintain the inter-pass temperature. The significance of fluid flow in the weld pool was neglected. The magnitude of the moving heat flux was adjusted in some cases to get a better match with the experimental thermal history. The thermal solution in ABAQUS is solved using the 'Newton–Raphson' method.
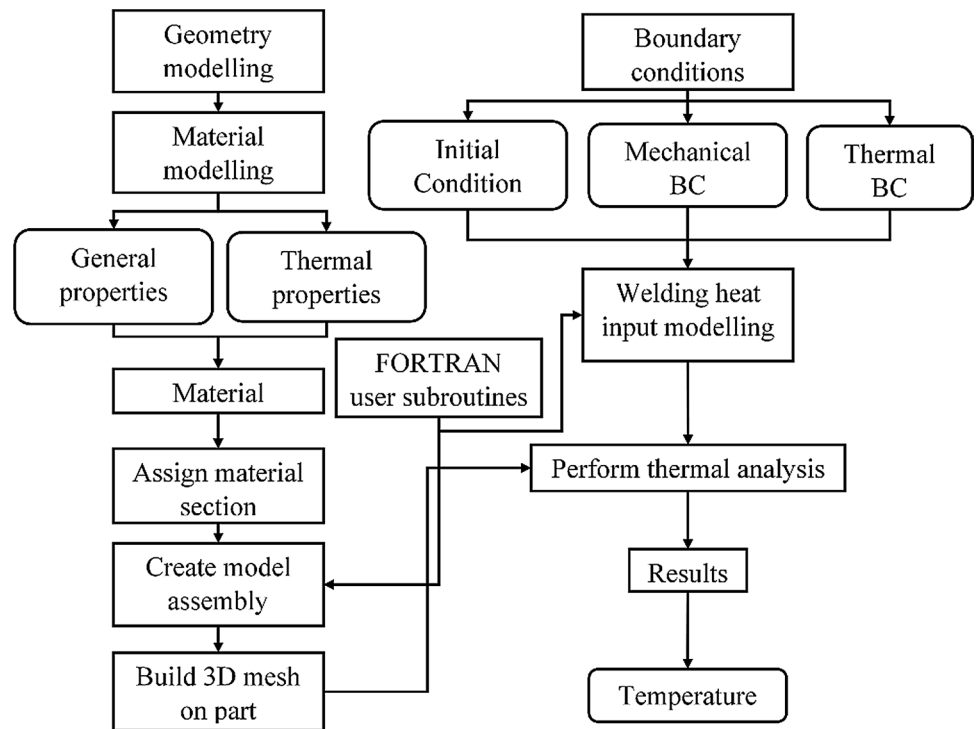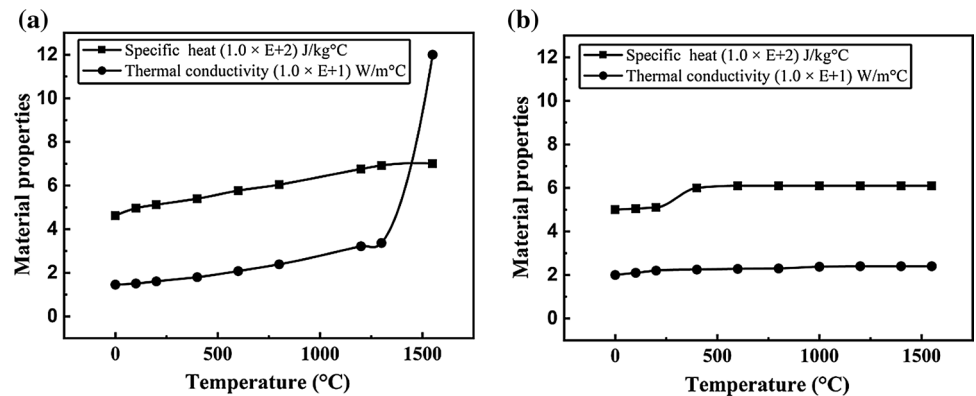
Fig. 3 Steps involved in computational modeling

Fig. 4 Temperature-dependent properties **a** SS304L **b** ER309L

3.1 Element death and birth

In the case of heterogeneous welding, the external filler material is added continuously from the moving welding torch. So, in this analysis, elements were added in the path of moving heat source to replicate the practical welding scenario. This procedure of filler material deposition in the numerical model was performed using element death and birth technique. The inactive materials of future passes may not get fit into distorted geometry of the weld groove due to previously deposited passes. So, while element activation, in an attempt to fit into the distorted geometry, stresses may build up in the subsequent passes. This problem can be sorted by an approach of keeping deactivated elements at a 'softening temperature' which decreases the stiffness and yield value of the elements to keep them thermal strain-free [16]. In some cases, elements assumed to be kept deactivated are given a value of thermal conductivity similar to that of air. At the time of their activation, the thermal conductivity values are then changed to that of weld metal [17]. In this study, 'UEPACTIVATIONVOL' user subroutine was used for element activation where elements are held at some 'annealed' state, which attributes zero stress, strain, conduction, etc. The centroids of the elements were kept aligned with the torch path, and elements got activated when the centroid of any element came within a certain distance close to the front head of the moving heat source. The shape and size of the weld beads were designed roughly to maintain simplicity in the modeling. An alternate welding sequence was followed in both the experimental and numerical approaches.

3.2 Thermal analysis

The present FE models of gas metal arc welded joints follow standard Fourier's law of heat conduction as the governing equation for transient heat transfer analysis. It is given by.

$$\rho c \frac{\partial T}{\partial t} = \frac{\partial}{\partial x}\left[k_x \frac{\partial T}{\partial x}\right] + \frac{\partial}{\partial y}\left[k_y \frac{\partial T}{\partial y}\right] + \frac{\partial}{\partial z}\left[k_z \frac{\partial T}{\partial z}\right] + Q \qquad (1)$$

where ρ and c are density and specific heat of stainless steel, respectively. The instantaneous temperature, $T = T(x, y, z, t)$, is a function of time t in the local coordinates x, y, and z. As stainless steel may be assumed to be isotropic, conductivity in different directions was assumed to be equal; $k_x = k_y = k_z = K$

The FE model maintains the basic energy balance equation in the form of integral formulation for the entire volume of the model. It follows the 'weak form' attained from the principle of virtual temperatures. It can be expressed as below

$$\int_V \bar{T}(\rho c)T' \mathrm{d}V + \int_V \bar{T}' k T' \mathrm{d}V = \int_S \bar{T} q \mathrm{d}S + \int_V \bar{T} r \mathrm{d}V \qquad (2)$$

where V is the volume of the model, $\bar{T}$ is virtual temperature distribution, q is the magnitude of heat flux per unit area, S is the surface area of the model, and r is the amount of external heat supplied to the body per unit volume.

Conventional Goldak double ellipsoidal heat source model was adapted using user subroutine 'UMDFLUX' [18, 19]. The below equations express it.

For the frontal part,

$$Q(x, y, z, t) = \frac{6\sqrt{3}f_f Q_w}{abc_f \pi \sqrt{\pi}} \cdot e^{-3\frac{x^2}{a^2}} \cdot e^{-3\frac{y^2}{b^2}} \cdot e^{-3\frac{z^2}{c_f^2}} \qquad (3)$$

For rear end part,

$$Q(x, y, z, t) = \frac{6\sqrt{3}f_r Q_w}{abc_r \pi \sqrt{\pi}} \cdot e^{-3\frac{x^2}{a^2}} \cdot e^{-3\frac{y^2}{b^2}} \cdot e^{-3\frac{z^2}{c_r^2}} \qquad (4)$$

where Q is the amount of instantaneous heat at any particular point in the weld axis at time t in the domain $Q(x, y, z, t)$ as a function of the local coordinates x, y, and z of the double ellipsoidal model. Q_w is the welding heat input estimated from the welding input current, voltage, and arc efficiency (80%) [20]. f_f and f_r is the fraction of heat dispersed in the front and rear head of the moving heat source, respectively. It is assumed that $f_f + f_r = 2$. The parameters of the heat source were defined as $f_f = 0.6$, $f_r = 1.4$, $a = 6$, $b = 7$, $c_f = 6$ and $c_r = 24$ [21]. Figure 5 shows an example of a typical moving heat source along the weld axis in the conventional groove weld joint.

Heat losses during and after welding operation were assumed to be dominated by convection and radiation. Both of these boundary conditions were employed for the entire outer surface of the models as shown in Fig. 6. Convection was kept limited only for the base material. Linear Newtonian convective cooling can be expressed as

$$Q_c = -h_c(T_s - T_i) \qquad (5)$$

where h_c is heat transfer coefficient assumed as 15×10^{-6} W/mm² °C [22], T_s is the surface temperature and T_i is the ambient room temperature which was taken as 28 °C. As radiation comes into consideration at elevated temperature; it was assumed for the weld and its adjacent region. Radiation is expressed by means of Stefan–Boltzmann law as

$$Q_r = -\in \sigma\left\{\left(T_s + 273.15\right)^4 - \left(T_i + 273.15\right)^4\right\} \qquad (6)$$

where $\in$ is emissivity (0.8) and σ is Stefan–Boltzmann constant. Instantaneous amplitude was preferred for both the thermal boundary conditions. Initially, the room temperature

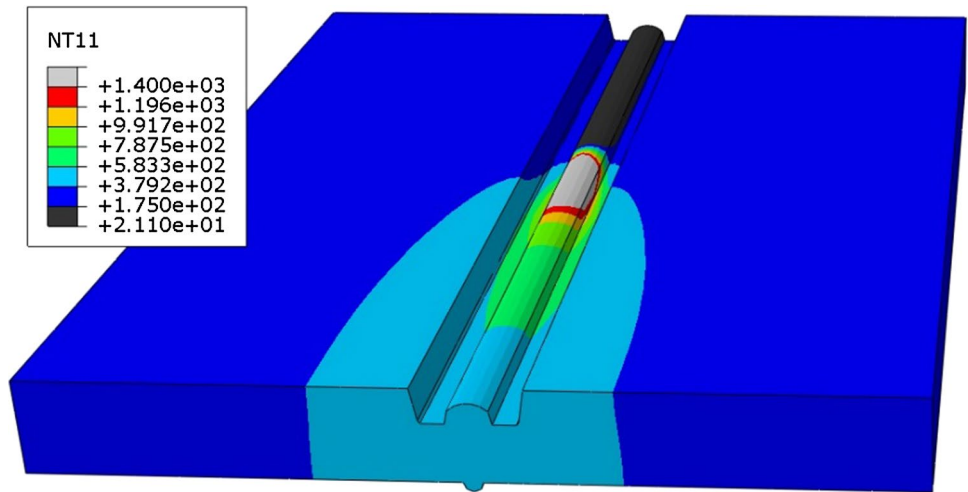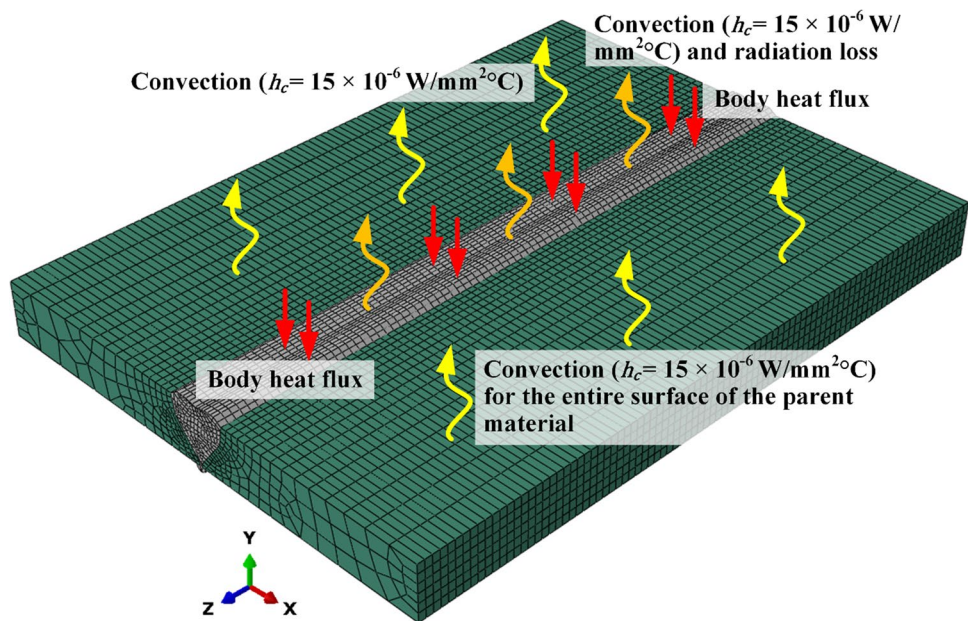**Fig. 5** Moving heat source in conventional groove joint

Fig. 6 Thermal boundary conditions

was selected as the predefined temperature of the base plates, and it got modified by the solver simultaneously as the analysis progressed.

3.3 Validation of the numerical model

The mesh sensitivity study was conducted by analyzing the correlation between the total number of elements, and the peak melting temperature attained in the weld pool during the thermal analysis. It can be seen from Fig. 7 that with an increase in the total number of elements, the peak melting temperature at the weld zone also increased significantly. However, after acquiring a certain number of elements, the peak temperature did not change much and remained constant after employing more than 36,000 total number
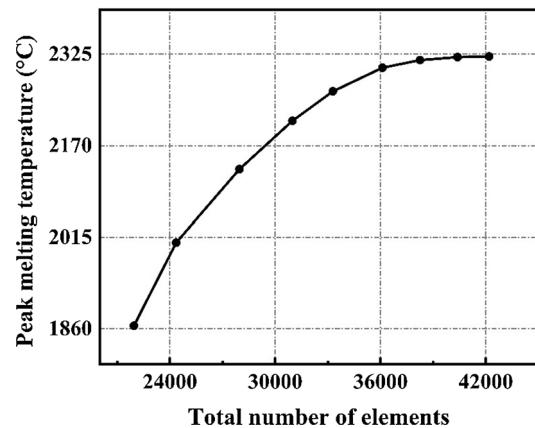

Fig. 7 Mesh sensitivity study in the conventional groove weld

of elements. The study was performed for the conventional groove weld, and a similar meshing scheme was also followed for the narrow groove weld.

It is necessary to validate the thermal solution with the experimental temperature history to ensure the efficiency of the prediction model. It can be supported by comparing the temperature distribution at any specific nodal point with the temperature data acquired from the attached thermocouple during the practical welding operation. Figure 8a, b shows the temperature history as a function of time for both the weld samples. A reasonably close match of the thermal history was achieved between the predicted thermal profile and experimentally obtained temperature data.

4 Results and discussion

4.1 Temperature contours

The temperature contour profile of the weld cross section distinguishes the fusion zone from the base material. The contour profiles shown in Fig. 9a, b were obtained along the cross section on a plane perpendicular to the longitudinal

axis and bisecting the axis (when the plane was experiencing peak temperature). The temperature contours represent the root pass, first pass, and the final pass for both the joints. The grey area of the weld cross section represents the fusion zone. It can be observed from the figures that the temperature of the weld zone reached well above the melting temperature (1400 °C) of the filler material. The fusion boundary conjointly attained the melting temperature, and overall, it signifies the successful fusion of the weld material. Besides, from the contour figures, the extent of HAZ adjacent to the fusion boundary can also be estimated.

4.2 Transient thermal analysis

In the case of single-pass welding, it is comparatively easier to detect the IGC-prone region as the base material undergoes a single thermal cycle which encounters zero effect of other thermal cycles. However, in multipass welding, the HAZ endures multiple thermal cycles, which alters the effect of former cycles. Figure 10a, b represents the transient temperature history of the HAZs corresponding to the final weld pass of both the weld joints. Based on the nodal points, the entire width of the HAZs was scattered into small chunks,

Fig. 8 Thermal cycles of last two passes **a** conventional groove weld **b** narrow groove weld
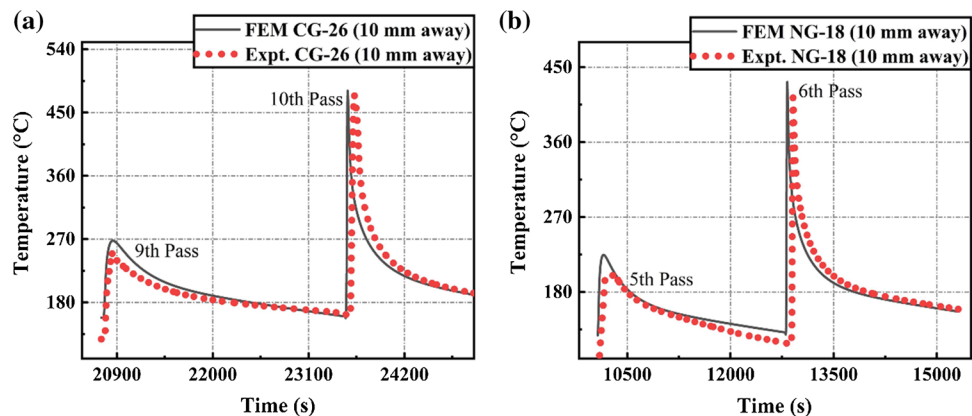

Fig. 9 Temperature contours **a** conventional groove weld, **b** narrow groove weld
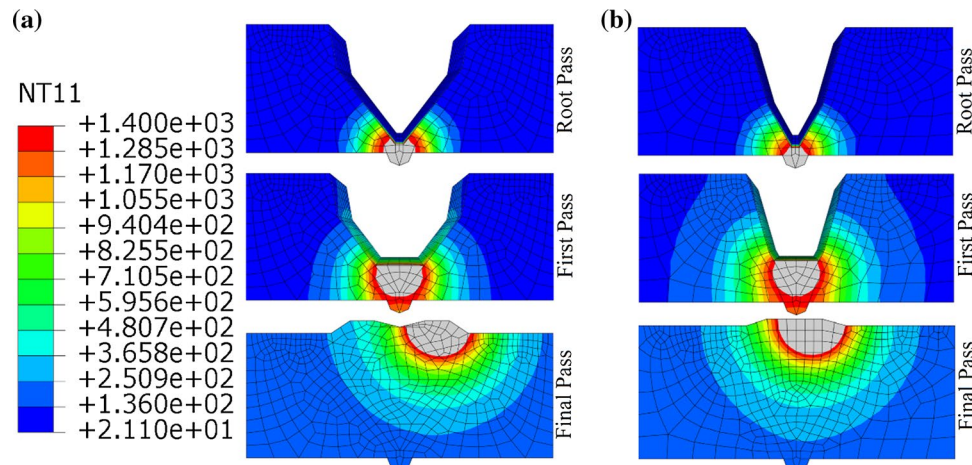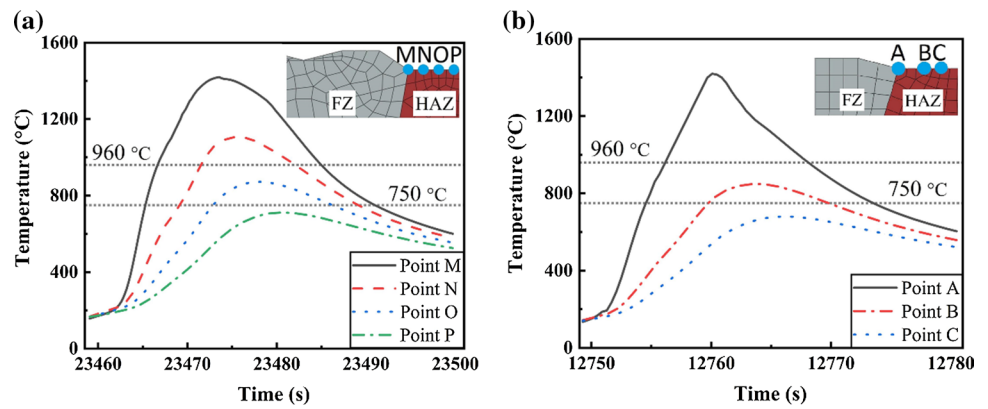
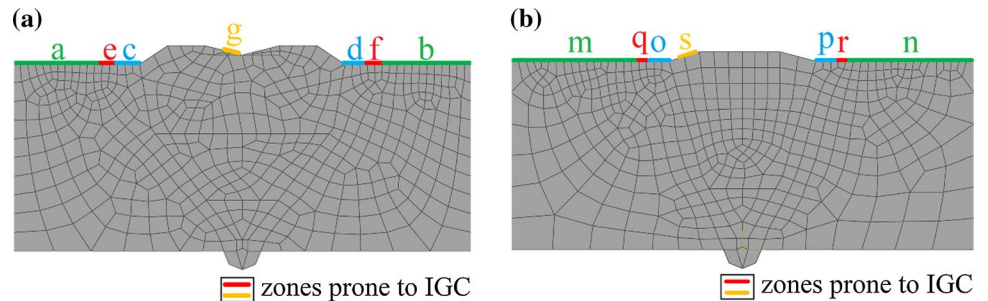**Fig. 10** Temperature history of different points at the HAZ **a** conventional weld, **b** narrow weld

and those were represented using alphabets, as shown in Fig. 10a, b. The zone of material where the peak temperature reached during the thermal cycling caused by welding lies between the ranges of 500–960 °C, which is identified as the overall sensitization zone. However, not the entire zone will be prone to the IGC attack. Out of this zone, the subzone that has undergone a peak temperature of thermal cycling, in the range of 750–960 °C, is classified as the zone of weld decay having maximum proneness to IGC attack, as per the findings of a prior work undertaken by Lee and Chen [5]. Hence, the range 750–960 °C is fixed for identifying the zone prone to IGC attack. It can be noticed that sections M, N, and P of the conventional weld, and sections A and C of the narrow weld, did not encounter the IGC-prone temperature limits, whereas section O of conventional weld and section B of the narrow weld were found to be in the IGC sensitive temperature range. Nodes M, N, O, and P are, respectively, 0, 2, 4, and 6 mm away from the fusion boundary. On the other hand, nodes A, B, and C are 0, 3, and 5 mm away from the fusion boundary. But, as it is multipass welding, the effect of the final thermal cycle is not enough to determine the IGC-prone zones; the former cycles must be taken into consideration. The complete temperature history of each region was further investigated for both the welded samples to determine the IGC sensitive regions. All the thermal histories were captured in the mid-length of the weld and there were no significant variations observed with those at the start and end of the weld length.

4.2.1 Thermal history of different zones in HAZ

The zones prone to intergranular corrosion can be determined in multipass welded joints based on the following three conditions. (1) The peak temperature of any particular zone should remain below the lower limit (750 °C) of the IGC temperature bracket during the entire welding process to avoid chromium carbide precipitation. (2) The peak temperature of any specific zone must cross the upper limit (960 °C) of the IGC temperature range throughout the complete welding operation to avoid the formation of any precipitation; or else, notably the final thermal cycle should achieve peak temperature higher than 960 °C. So, at least if the final thermal cycle crosses the maximum temperature boundary of IGC, that particular zone gets heat-treated, and the soluble phases dissolve in the matrix. (3) Finally, the chances of chromium carbide precipitation increase when the peak temperature of any thermal cycle falls within the IGC temperature range, and it remains below 960 °C in the subsequent weld thermal cycles. Different zones of both the weld groove joints enduring contrasting thermal cycles can be distinguished significantly from Fig. 11a, b. The temperature history of these different zones of conventional weld adjacent to the fusion boundary was evaluated from the thermal analysis, as shown in Fig. 12. It was observed that zones 'a' and 'b' encountered much lower temperature peaks, which are below 750 °C, whereas zones 'c' and 'd' went through

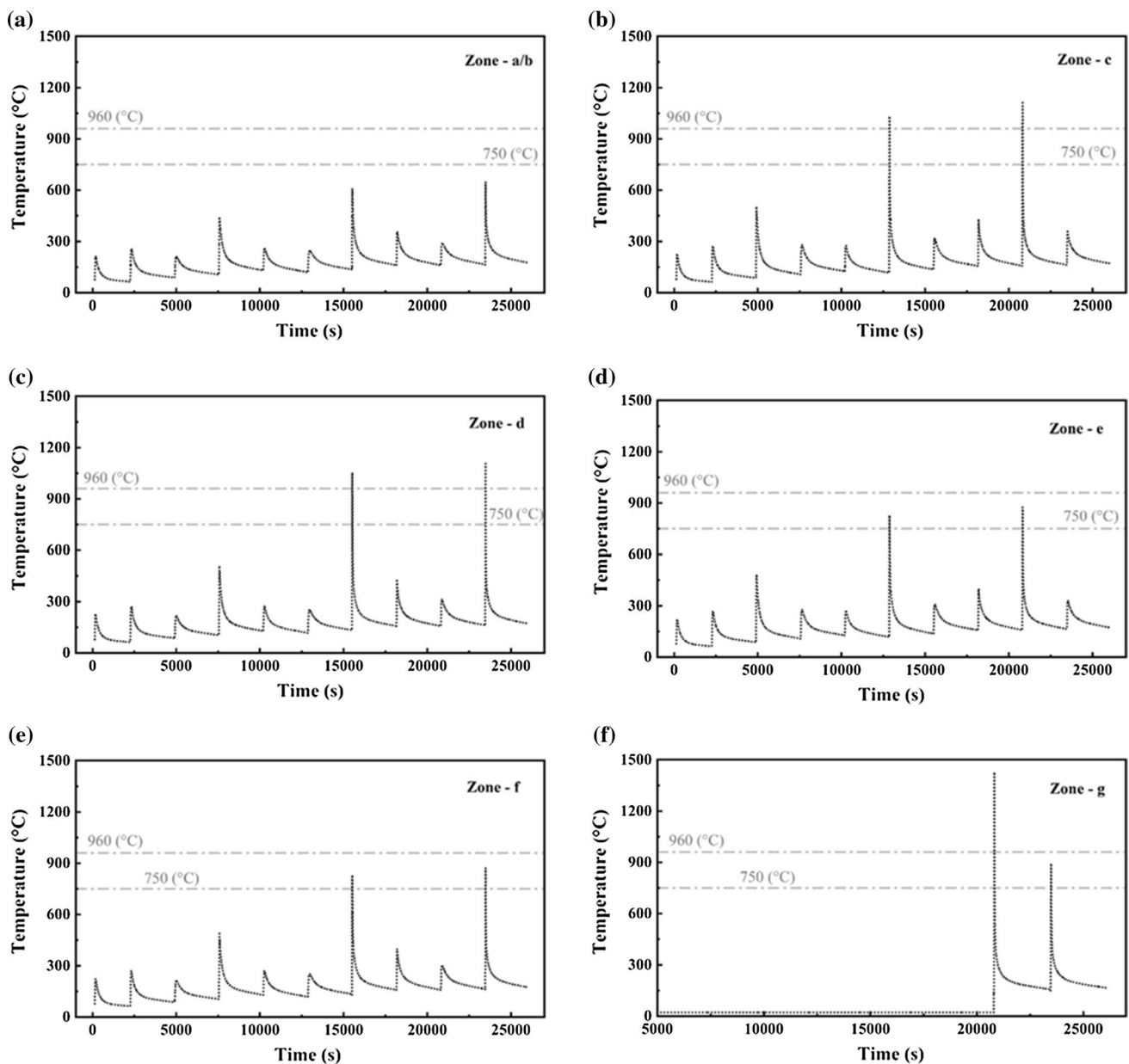**Fig. 11** Zones sensitive to IGC **a** conventional weld joint, **b** narrow weld joint

Fig. 12 Temperature history of different zones of conventional weld; **a** temperature history at zone a/b, **b** temperature history at zone c, **c** temperature history at zone d, **d** temperature history at zone e, **e** temperature history at zone f, **f** temperature history at zone g

elevated thermal exposure above 960 °C in the consecutive weld passes. In these cases, the zones either experienced a temperature higher than the upper limit or remained below the lower limit of the IGC temperature range. So, the chances of chromium carbide precipitation in these zones are comparatively small. It can also be noticed that zones 'e' and 'f' experienced peak temperatures within the IGC temperature bracket and hence can be distinguished to be IGC sensitive zones. Similarly, it can be observed that during the 9th weld pass, zone 'g' experienced melting

temperature, but the final weld thermal cycle went through the intergranular corrosion temperature limits making the zone 'g' also inclined to IGC. The narrow weld joint also endured different thermal cycles in distant zones, as represented in Fig. 13. It can be noticed that the zones 'm,' 'n,' 'o,' and 'p' of the HAZs of narrow groove weld are on the safer side from the chromium carbide precipitation. However, it is also evident that zones 'q,' 'r,' and 's' are exposed to IGC temperature bracket, which may make them susceptible to IGC.

(a)

(b)

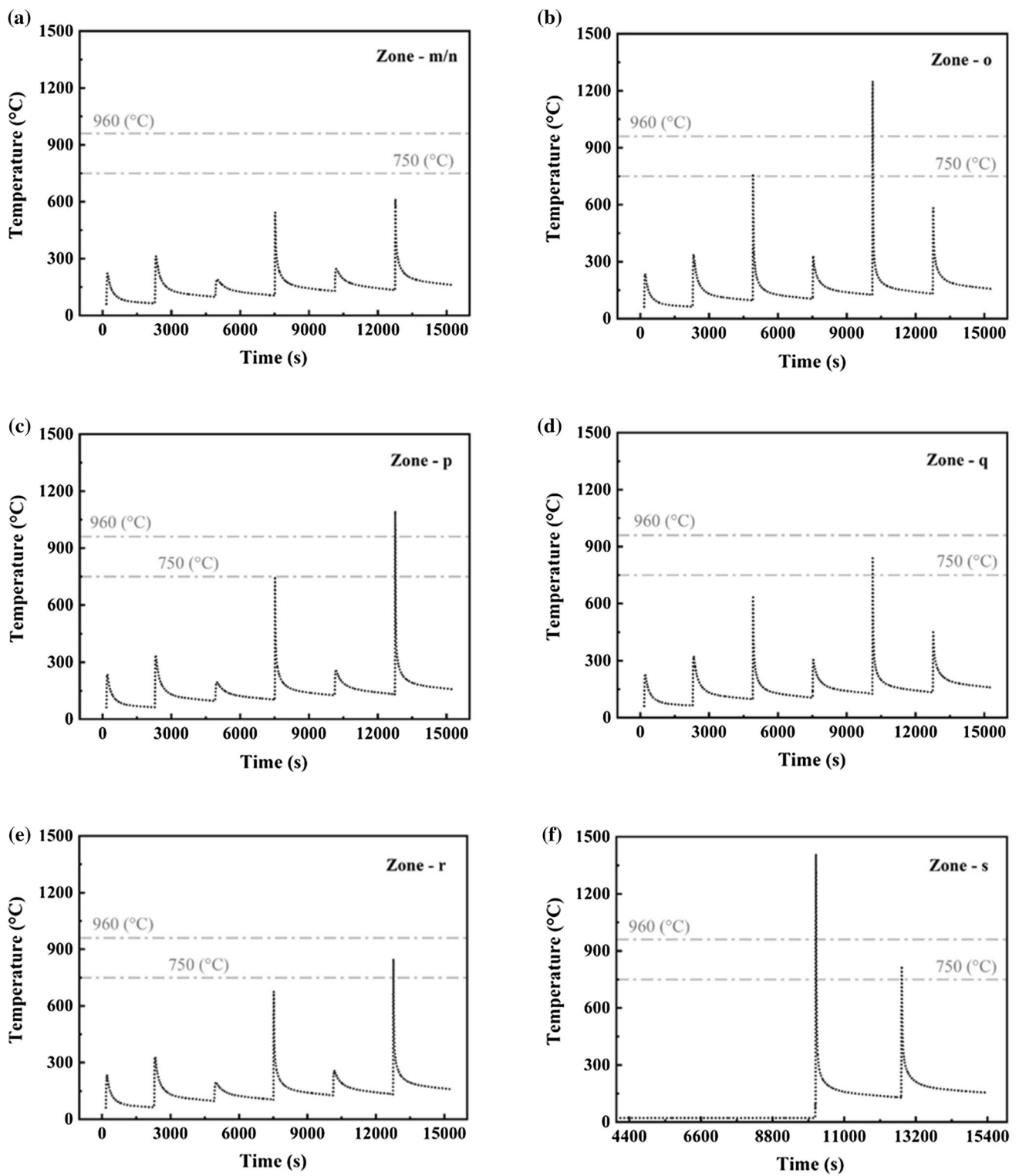**(c)**

(d)

(e)

(f)

Fig. 13 Temperature history of different zones of the conventional weld; **a** temperature history at zone m/n, **b** temperature history at zone o, **c** temperature history at zone p, **d** temperature history at zone q, **e** temperature history at zone r, **f** temperature history at zone s
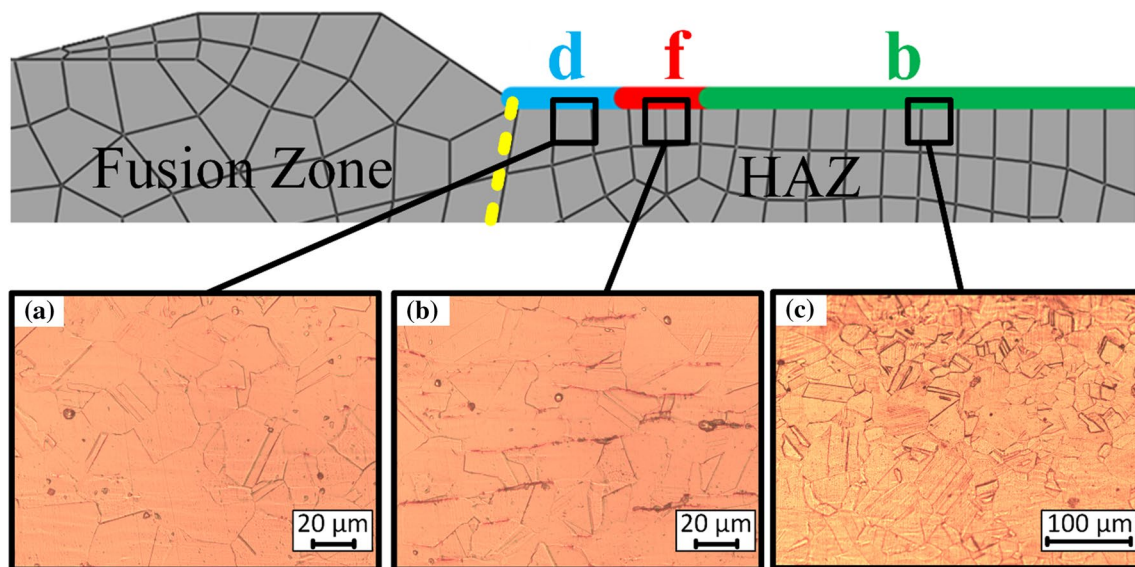
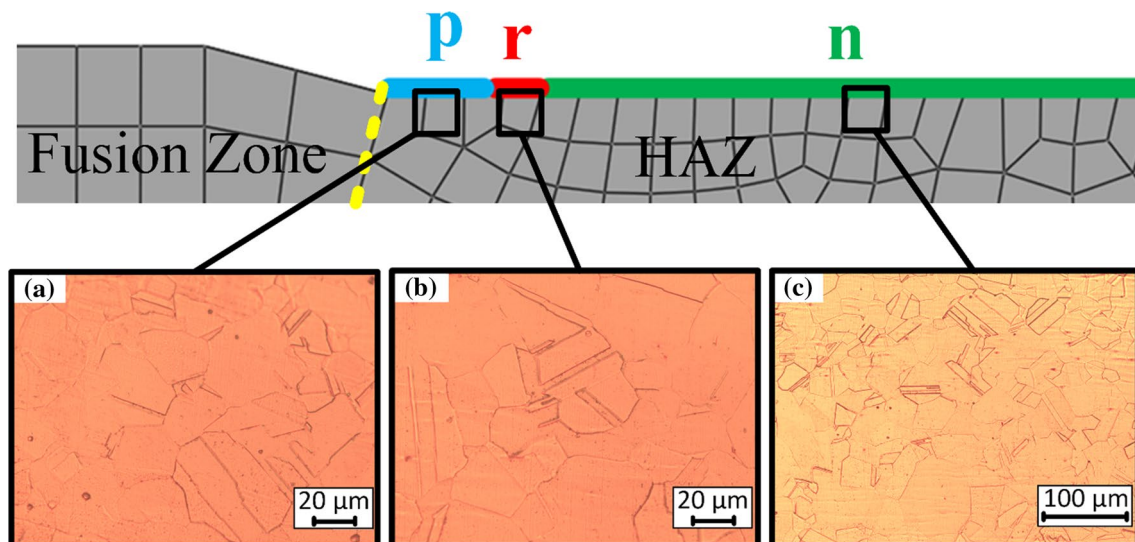**Fig. 14** Microstructures of the HAZ of conventional groove weld **a** zone 'd' **b** zone 'f' **c** zone 'b'

Fig. 15 Microstructures of the HAZ of narrow groove weld **a** zone 'p' **b** zone 'r' **c** zone 'n'

4.2.2 Evaluation of microstructure

The sensitization tendency of the weld groove geometries was further investigated from the weld micrographs. Figures 14 and 15 represent the microstructural images of the HAZs of both the weldments after oxalic acid etching following ASTM A262 practice. A similar microstructural observation has also been reported by Pandey [23]. Figure 14a shows apparent step structures (no ditches at the grain boundaries) with few deep end grain pits, and shallow etch pits near the fusion boundary at the zone 'd' which is free from the susceptibility of IGC. Here the number of possible sites of carbide formation is less because of higher peak temperature, which dissolves Cr-carbides in the matrix. Zone 'f' is the place where the temperature reaches within the IGC temperature bracket. Figure 14b shows a few dual structures (no single grain entirely surrounded by ditches) around the zone 'f,' which clearly indicates the nucleation of Cr-carbides. These nuclei of carbides reduce the corrosion resistance by actively influencing LTS. At the zone 'b,' step structures were observed with no sign of Cr-carbide precipitation, as shown in Fig. 14c. From Fig. 15 it is also evident that no
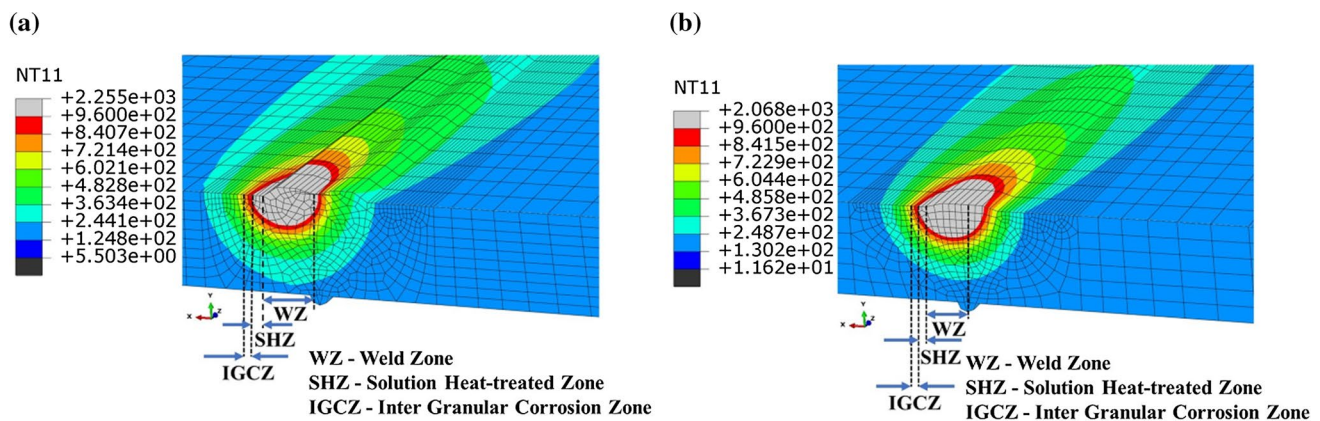
(a)

(b)

Fig. 16 The cross-sectional view of transient temperature contours **a** conventional groove weld **b** narrow groove weld

Cr-carbide precipitation was observed across the HAZ of the narrow groove weld; only step structures were noticed.

4.2.3 Total time spent within IGC temperature range

The formation of precipitates is mostly time-dependent, and thus, time plays a significant role in the generation of IGC sensitive zones. During heating and cooling of welding, precise sections of the base material and small portions of the weld material undergo a few specific thermal cycles which reach the sensitization temperature range and stay within limits for a certain duration (hold time). The enrichment of chromium carbide precipitates rises with an increase in the hold time within the sensitization temperature limits [24]. So, the chances of $Cr_{23}C_6$ precipitation get decreased with reduction in hold time. The duration of this hold time can be calculated using simulated results. In conventional weld, the zones 'e,' 'f,' and 'g' experienced the IGC temperature range for 30, 29, and 14 s, respectively. On the other hand, in the narrow weld joint, the zones 'q,' 'r,' and 's' endured the IGC temperature range for 10, 9, and 8 s. The distance of the IGC zone from the fusion boundary is shown in Fig. 16a, b for conventional and narrow groove design, respectively, which shows that the size of the solution heat-treated zone got decreased in the narrow groove weld joint. The width of the IGC sensitive zone was observed to be 2.1 mm and 1.8 mm in conventional and narrow grooved welds, respectively.

5 Conclusions

The methodology to minimize the propensity of IGC in multipass welds of commercial-grade SS304L has been illustrated. Thermal cycles exhibited during heating and cooling of two welded joints of different groove geometries were evaluated using numerical modeling, and the results were verified with the experimental data. The

following conclusions can be summarized from the present investigation:

- The three-dimensional transient numerical model with temperature-dependent material properties successfully predicted the weld thermal cycles with a reasonably close match with the temperature history obtained experimentally.
- The results obtained from the thermal analysis suggest that the time spent within the IGC temperature bracket is comparatively higher in conventional groove weld, whereas narrow groove weld exhibited around 50% significant decrease in hold time.
- Oxalic acid etch test revealed dual structure at the HAZ of the conventional groove weld.
- The IGC-sensitive zone comparatively appears to be broader in the conventional groove weld.

References

1. Verma J, Taiwade RV, Khatirkar RK, Sapate SG, Gaikwad AD. Microstructure, mechanical and intergranular corrosion behavior of dissimilar DSS 2205 and ASS 316L shielded metal arc welds. Trans Indian Inst Met. 2017;70:225–37. https://doi.org/10.1007/s12666-016-0878-8.
2. Xin J, Song Y, Fang C, Wei J, Huang C, Wang S. Evaluation of inter-granular corrosion susceptibility in 316LN austenitic stainless steel weldments. Fusion Eng Des. 2018;133:70–6. https://doi.org/10.1016/j.fusengdes.2018.05.078.
3. Kessal BA, Fares C, Meliani MH, Alhussein A, Bouledroua O, François M. Effect of gas tungsten arc welding parameters on the corrosion resistance and the residual stress of heat affected zone. Eng Fail Anal. 2020;107:104200. https://doi.org/10.1016/j.engfailanal.2019.104200.
4. Javidi M, Haghshenas SMS, Shariat MH. CO2 corrosion behavior of sensitized 304 and 316 austenitic stainless steels in 3.5wt% NaCl solution and presence of H2S. Corros Sci. 2020;163:108230. https://doi.org/10.1016/j.corsci.2019.108230.

5. Lee HT, Te Chen C. Numerical and experimental investigation into effect of temperature field on sensitization of AISI 304 in butt welds fabricated by gas tungsten arc welding. Mater Trans. 2011;52:1506–14. https://doi.org/10.2320/matertrans.m2011071.

6. Kou S. Corrosion-resistant materials: stainless steels. In: Kou S, editor. Welding Metallurgy. 2nd ed. Hoboken, New Jersey: Wiley; 2002.

7. Sandusky DW, Okada T, Saito T. Advanced boiling water reactor materials technology. Mater Perform. 1990;29:66–71.

8. Singh PK, Bhasin V, Ghosh AK, Kushwaha HS. Structural integrity of main heat transport system piping of AHWR. BARC News Lett. 2008;299:2–18.

9. Kekkonen T. Metallurgical effects on the corrosion resistance of a low temperature sensitized weld AISI type 304 stainless steel. Corros Sci. 1985;25:821–36.

10. Schmidt CG, Caligiuri RD, Eiselstein LE, Wing SS, Cubicciotti D. Low temperature sensitization of type 304 stainless steel pipe weld heat affected zone. Metall Trans A Phys Metall Mater Sci. 1987;18A:1483–93. https://doi.org/10.1007/BF02646660.

11. Singh R., Das G., Suman S., Singh PK. Response of weld joints in stainless steel 304LN pipe to low temperature sensitization. In: IIW IC, Chennai, 2008, pp. 551–556.

12. Hsu CH, Chen TC, Huang RT, Tsay LW. Stress corrosion cracking susceptibility of 304L substrate and 308L weld metal exposed to a salt spray. Materials. 2017;10:1–14. https://doi.org/10.3390/ma10020187.

13. Giri A, Mahapatra MM, Sharma K, Singh PK. A study on the effect of weld groove designs on residual stresses in SS 304LN thick multipass pipe welds. Int J Steel Struct. 2017;17:65–75. https://doi.org/10.1007/s13296-016-0118-4.

14. Kim IS, Lee JS, Kimura A. Embrittlement of ER309L stainless steel clad by σ-phase and neutron irradiation. J Nucl Mater. 2004;329–333:607–11. https://doi.org/10.1016/j.jnucmat.2004.04.104.

15. Nadimi S, Khoushehmehr RJ, Rohani B, Mostafapour A. Investigation and analysis of weld induced residual stresses in two dissimilar pipes by finite element modeling. J Appl Sci. 2008;8:1014–20.

16. Brickstad B, Josefson BL. A parametric study of residual stresses in multi-pass butt-welded stainless steel pipes. Int J Press Vessel Pip. 1998;75:11–25. https://doi.org/10.1016/S0308-0161(97)00117-8.

17. Yaghi A, Hyde TH, Becker AA, Sun W, Williams JA. Residual stress simulation in thin and thick-walled stainless steel pipe welds including pipe diameter effects. Int J Press Vessel Pip. 2006;83:864–74. https://doi.org/10.1016/j.ijpvp.2006.08.014.

18. Goldak J, Chakravarti A, Bibby M. A new finite element model for welding heat source. Metall Trans B. 1984;15B:299–305.

19. Deng D, Murakawa H. Numerical simulation of temperature field and residual stress in multi-pass welds in stainless steel pipe and comparison with experimental measurements. Comput Mater Sci. 2006;37:269–77. https://doi.org/10.1016/j.commatsci.2005.07.007.

20. Gannon L, Liu Y, Pegg N, Smith M. Effect of welding sequence on residual stress and distortion in flat-bar stiffened plates. Mar Struct. 2010;23:385–404. https://doi.org/10.1016/j.marstruc.2010.05.002.

21. Gery D, Long H, Maropoulos P. Effects of welding speed, energy input and heat source distribution on temperature variations in butt joint welding. J Mater Process Technol. 2005;167:393–401. https://doi.org/10.1016/j.jmatprotec.2005.06.018.

22. Deng D, Kiyoshima S. FEM prediction of welding residual stresses in a SUS304 girth-welded pipe with emphasis on stress distribution near weld start/end location. Comput Mater Sci. 2010;50:612–21. https://doi.org/10.1016/j.commatsci.2010.09.025.

23. Pandey C. Mechanical and metallurgical characterization of dissimilar P92/SS304 L welded joints under varying heat treatment regimes. Metall Mater Trans A Phys Metall Mater Sci. 2020;51:2126–42. https://doi.org/10.1007/s11661-020-05660-0.

24. Warikh M, Rashid A, Gakim M, Rosli ZM, Azam MA. Formation of $Cr_{23}C_6$ during the sensitization of AISI 304 stainless steel and its effect to pitting corrosion. Int J Electrochem Sci. 2012;7:9465–77.